ANKE Internal Report

Luminosity determination for the February 01 deuteron breakup beam time

S.Yaschenko, S.Dymov, A.Kacharava,
V.Komarov, G.Macharashvili, A.Petrus,
F.Rathmann, H.Seyfarth, Yu.Uzikov

Jülich, May 2002

1 Introduction

During the *pd* breakup beam time (February 2001) experimental data were obtained with the deuteron cluster target at proton beam energies of 600, 700, 800, 950, 1350 and 1900 MeV. In this report the procedure of luminosity determination for this beam time is described. The luminosity for all the runs was calculated using *pd* forward scattering with one proton registered in the ANKE Forward detector (FD). The results are compared with the luminosity determined using *pd* backward scattering with one deuteron registered in FD.

2 Method

The procedure of luminosity determination consists of the following parts.

1. Selection of events with one track in the Forward detector and reconstructed momentum.

2. Particle type separation by energy losses in two planes of FD scintillation hodoscope.

3. Event selection for each reaction of interest (*pd* forward scattering and *pd* backward scattering) on the basis of momentum spectra for different polar angles (with 1 degree bins) including MWPC efficiency correction of momentum spectra.

4. Calculation of counting rates from momentum peaks for different polar angles with background subtraction and DAQ dead time correction.

5. Determination of luminosities values using theoretically calculated (and experimental measured) differential cross sections, including values of the Forward detector acceptance.

6. Final luminosity calculation by averaging over polar angles.

2.1 Luminosity obtained from *pd* forward scattering

2.1.1 Event selection in Forward Detector

The event selection of *pd* forward scattering was done among single track events in the data taken with FD trigger. (Multiple track events are seldom.) For track reconstruction all three FD MWPC were used (3MWPC algorithm). In the begining only the first and third FD MWPC (2MWPC algorithm) were used because the algorithm of 3 chamber track reconstruction was not yet developed at that time. The horizontal and vertical limitations on track coordinates at the D2 exit window and vertical cut on the target position were applied [1].

Because this process has a very large cross section and is not suppressed much by the acceptance of setup, it can be easily observed in the momentum and angular-momentum spectra and is thus easily selectable. Nevertheless, the energy loss cuts were applied to suppress deuteron background from the $pd \to dn\pi^+$ reaction.

2.1.2 Particle type separation

The protons and deuterons can be separated by energy loss in the scintillation counters. A code for the transformation of pulse height amplitudes into energy loss has been used in this procedure. The particle mass are calculated from the energy loss for each of the two planes of Forward hodoscope and momentum. In order to take into account the information from both hodoscope planes we used the following method: In Fig. 1 the 2D plot of mass using energy losses in the first and second plane of the Forward hodoscope is shown. It is seen that using the cut shown (lines) it is possible to select protons (or deuterons). Such a cut corresponds to the simple cut in a one dimension distribution of minimal masses $m = min(m1, m2)$ (Fig. 2). In Figs. 3, 4 the results of cuts on minimal mass distribution applied for proton and deuteron selection are shown in distribution of the energy losses vs momentum.

2.1.3 MWPC efficiency correction

The procedure of efficiency of ANKE Forward proportional chambers (FMWPCs) is described in Ref. [3]. For each event the track efficiency was calculated and used as a correction factor in analyzed momentum distributions. Track efficiency vs polar angle is shown in Figs. 5, 6 for 2 FMWPC and 3 FMWPC track reconstruction algorithms.

2.1.4 Counting rate calculation with background subtraction and DAQ dead time corrections

After selection of protons by energy loss the momentum spectra in different polar angle intervals (1 degree bins) in the range $5 - 10$ degree were analyzed. The peak region of the momentum spectra was fitted by a sum of a gauss distribution and an inclined line, events were selected within 2σ from the fitted average momentum value. In Fig. 7 an example of such a fit is shown. Then the counting rates for the different polar angles were calculated taking into account the DAQ dead time correction [1]. DAQ efficiensy depended on the trigger conditions and was in the region 50%–90%.

2.1.5 Theoretical cross section and acceptance calculations for the setup

The cross sections of the pd forward scattering were calculated [2] in approximation of Glauber-Sitenko theory. The pd scattering cross section consists of elastic and inelastic terms. It is not possible to separate these processes experimentally in ANKE

FD due to the very similar kinematical parameters of the forward protons, and the momentum and angular resolution of the FD. Therefore, the theoretical calculations of differential cross sections took into account the both processes. It is shown that the agreement of results of calculations agree with existing experimental data to about 15% accuracy. In Table 1 the results of comparisson of theoretical calculations with existing experimental data (in ANKE angle acceptance region) is shown.

Table 1. Comparisson of theoretical calculations with experimantal data.

T_p, MeV	Θ_{lab}, deg	$d\sigma^{exp}/d\Omega_{cm}, mb/sr$	$d\sigma^{theory}/d\Omega_{cm}, mb/sr$	diff, %
600	10.9	11.9 $\pm$ 1.9	12.09	1.6
792	11.2	14.9 $\pm$ 4.8	12.25	-17.8
1016	6.1	60 $\pm$ 3	47.3	-21.2
1016	6.7	45 $\pm$ 4	40.7	-9.6
1016	8.5	27 $\pm$ 3	22.4	-17.0
1016	9.1	23 $\pm$ 3	17.7	-23.
1016	9.7	18 $\pm$ 3	14.4	-20.
1016	10.9	10 $\pm$ 1.5	8.9	-11.
1995	4.5	54.5 $\pm$ 2	57.9	6.2
1995	5.7	28.2 $\pm$ 1.5	28.3	0.3
1995	7.2	11.3 $\pm$ 0.5	10.4	-8.0
1995	7.7	8.5 $\pm$ 0.5	6.7	-21.
1995	8.2	5.7 $\pm$ 0.5	4.3	-24.
		$d\sigma^{exp}/dt, mb/(GeV/c)^2$	$d\sigma^{theory}/dt, mb/(GeV/c)^2$	
695	5.5	200. $\pm$ 1.	180.	-10.
695	9.5	100. $\pm$ 1.	108.6	8.6
695	11.7	60 $\pm$ 1.	72.	20.
956	5.6	30.0 $\pm$ 2.5	23.8	-20.6
956	7.3	51 $\pm$ 3	43.2	-15.3
956	8.6	62 $\pm$ 4	61.	-0.2
956	10.3	74 $\pm$ 4	80.	8.1
956	11.0	80.0 $\pm$ 5	85.5	6.8

The FD acceptance was calculated using a GEANT-based simulation program, that includes a realistic description of the D2 dipole and the FD. Measured magnetic field map was used (inside the measured volume) together with the calculated one (outside). Events with pd elastic kinematics were generated in polar angle interval of forward emitted proton ranging from $0 - 20$ degree and azimuth ϕ randomly distributed in the range of $0 - 2\pi$. The criteria for accepting an event during the simulation were:

– A particle emitted does not hit constructional elements of D2 (particularly the poles).

– Particle crosses the forward exit window of D2.

– Particle crosses the sensitive region of the forward MWPC1 ad MWPC2, that is, the number of wire hits calculated from the track crossing point coordinate is in the valid range.

– Particle crosses first and second planes of FD hodoscope, which corresponds to the hardware trigger condition.

As a result we obtained the dependence of the acceptance on the polar angle shown in Fig. 9. The limit values of θ coincide well with experimental data.

2.1.6 Luminosity calculation

Finally, using count rates and theoretically calculated differential cross sections, corrected to the FD acceptance, the luminosity for the different polar angle bins was calculated. In Fig. 10 (2 FMWPC reconstruction algorithm) and 11 (3 FMWPC reconstruction algorithm) the dependence of a luminosity on a polar angle is shown. Averaging the luminosity over the polar angle the mean luminosity values are obtained and listed in Tables 2–7 (2 FMWPC reconstruction algorithm) and 8–13 (3 FMWPC reconstruction algorithm).

The errors correspond to a root mean squared deviations of the luminosities, determined for individual angle bins. These errors were considered as one source of systematics. A second source is the accuracy of the theoretical calculations of cross section, estimated to be $\approx 15\%$. The statistical errors are negligible in comparison with the systematic ones. Significant dispersion of the luminosity value over the runs is evidently caused by the instability of the cluster target density during the beam time.

2.2 Luminosity determination using pd backward scattering

For event selection and momentum spectra analysis the procedure described above was used also for deuterons from pd backward scattering. After energy loss selection, clear peaks in the momentum spectra are seen for beam energies 600, 700 and 800 MeV (see for example Fig. 8). The momentum spectra in the range of the peak were fitted by Gaussian and linear function and the full number of events under Gaussian was used for the counting rate calculation. There are experimental data on $pd \to dp$ differential cross sections at proton beam energies of 433 MeV [4], 470 MeV [5], 582 MeV [6], 590 MeV [5], 792 MeV [7] and 800 MeV [8] available. The theoretical calculations of the differential cross sections, similar to [9], were carried out. The experimental and calculated theoretical data were transformed from the center-of-mass system to the laboratory system. In Figs. 13–18 a comparison of these calculations with existing experimental data is shown. The calculated cross sections are close to the experimental ones for the energies 582 MeV, 590 MeV and 800 MeV in the angular range of interest (from 7 to 11 degree). However, a slope of the angular dependence has a systematic tendency to being less for the calculated relative the experimental. Since we used the theoretical values of the cross sections for the luminosity calculation at the energies 600, 700 and 800 MeV this difference of the slope reflected in a rather large dispersion of the obtained luminosity values in different angular bins (see Fig. 12) and the appropriate large systematic error of the average values (the third column of Tables 2–4 and 8–10). Nevertheless, the average values of the luminosities obtained by the forward and backward scattering for different runs corresponds well, and the integrated luminosities are in agreement with accuracy of about 15%.

3 Results

In Tables 2–7 and 8–13 the results of luminosity determination for all the February 01 runs is presented. L_{forw} is the luminosity determined by pd forward scattering, L_{back} — by pd backward scattering. For each beam energy and each run integrated luminosity was calculated as well. In Table 14 all the correction factors and their uncertainties are summarised. Table 15 containes the comparison of luminosities obtained from forward and backward scattering data using 2 and 3 FWMPC track reconstruction algorithms. In Table 16 the integral luminosities are shown taking into account all correction listed in Table 14.

References

[1] S.Dymov et al., Luminosity estimation in $a0$ January 2001 beam time, 03.2001.

[2] Yu.Uzikov, Diffraction pd scattering at COSY energies. ANKE Internal report, 2001.

[3] S.Dymov, Determination of the FD MWPC efficiency. ANKE Internal report, 10.05.2001.

[4] N.E.Booth et al., Phys.Rev.D**4**, 1261(1971).

[5] J.C.Alder et al., Phys.Rev.C**6**, 2008(1972).

[6] E.T.Boschitz et al., Phys.Rev.C**6**, 547(1972).

[7] E.Gülmez et al., Phys.Rev.C**43**, 2067(1991).

[8] E.Winkelmann et al., Phys.Rev.C**21**, 2535(1980).

[9] Yu.Uzikov, Elem. Particl. and Nuclei, 29, 1405(1998)

Table 2. Luminosity for the beam energy 600 MeV (2 FMWPC).

Run number	L_{forw} [$cm^{-2}s^{-1} \cdot 10^{30}$]	L_{back} [$cm^{-2}s^{-1} \cdot 10^{30}$]	Time [s]
3412	0.046 ± 0.002	0.037 ± 0.014	1488.7
3414	0.140 ± 0.007	0.119 ± 0.028	2064.4
3415	0.525 ± 0.024	0.427 ± 0.082	4117.6
3416	1.087 ± 0.049	0.965 ± 0.142	583.2
3417	0.599 ± 0.032	0.396 ± 0.161	84.4
3418	0.482 ± 0.020	0.397 ± 0.073	6922.2
3419	0.688 ± 0.029	0.578 ± 0.097	3388.4
3420	0.784 ± 0.032	0.657 ± 0.091	969.5

Table 3. Luminosity for the beam energy 700 MeV (2 FMWPC).

Run number	L_{forw} [$cm^{-2}s^{-1} \cdot 10^{30}$]	L_{back} [$cm^{-2}s^{-1} \cdot 10^{30}$]	Time [s]
3442	0.405 ± 0.022	0.39 ± 0.09	3827.3
3443	0.33 ± 0.02	0.33 ± 0.07	4422.3
3453	0.200 ± 0.010	0.19 ± 0.03	7638.3
3454	0.41 ± 0.02	0.43 ± 0.06	3877.5
3455	0.43 ± 0.02	0.40 ± 0.10	3681.9
3456	0.38 ± 0.019	0.41 ± 0.06	2412.3
3457	0.17 ± 0.009	0.16 ± 0.04	8905.7
3458	0.396 ± 0.019	0.40 ± 0.06	3527.7

Table 4. Luminosity for the beam energy 800 MeV (2 FMWPC).

Run number	L_{forw} [$cm^{-2}s^{-1} \cdot 10^{30}$]	L_{back} [$cm^{-2}s^{-1} \cdot 10^{30}$]	Time [s]
3421	0.579 ± 0.033	0.590 ± 0.100	2600.3
3422	0.476 ± 0.028	0.390 ± 0.090	3677.4
3423	0.433 ± 0.025	0.426 ± 0.071	4644.0
3424	0.484 ± 0.027	0.399 ± 0.118	3082.1
3448	0.200 ± 0.013	0.197 ± 0.057	4414.4
3449	0.263 ± 0.016	0.249 ± 0.054	4733.0
3450	0.311 ± 0.020	0.288 ± 0.091	5282.1
3451	0.275 ± 0.017	0.252 ± 0.050	5317.9
3452	0.190 ± 0.012	0.110 ± 0.076	4546.4
3460	0.420 ± 0.026	0.395 ± 0.110	6683.9
3461	0.294 ± 0.024	0.270 ± 0.110	332.2
3462	0.409 ± 0.024	0.391 ± 0.065	7541.5
3463	0.352 ± 0.019	0.372 ± 0.137	2992.6

Table 5. Luminosity for the beam energy 950 MeV (2 FMWPC).

Run number	L_{forw} [$cm^{-2}s^{-1} \cdot 10^{30}$]	Time [s]
3430	0.020 ± 0.001	4715.7
3431	0.017 ± 0.001	1644.2
3433	0.020 ± 0.002	1645.5
3434	0.513 ± 0.023	3973.3
3435	0.446 ± 0.019	2685.9
3436	0.501 ± 0.023	4180.7
3437	0.439 ± 0.021	1429.0
3444	0.309 ± 0.018	3645.5
3445	0.312 ± 0.017	3525.8
3446	0.327 ± 0.018	3423.0
3447	0.332 ± 0.019	4266.9

Table 6. Luminosity for the beam energy 1350 MeV (2 FMWPC).

Run number	L_{forw} [$cm^{-2}s^{-1} \cdot 10^{30}$]	Time [s]
3425	0.526 ± 0.034	2262.3
3426	0.441 ± 0.026	3827.4
3427	0.356 ± 0.022	3664.9
3428	0.445 ± 0.025	301.7
3429	0.348 ± 0.021	4567.3

Table 7. Luminosity for the beam energy 1900 MeV (2 FMWPC).

Run number	L_{forw} [$cm^{-2}s^{-1} \cdot 10^{30}$]	Time [s]
3407	0.226 ± 0.018	1099.9
3408	0.388 ± 0.030	3917.3
3409	0.341 ± 0.025	4359.7
3410	0.625 ± 0.046	2168.4
3411	1.091 ± 0.079	1341.8

Table 8. Luminosity for the beam energy 600 MeV (3 FMWPC).

Run number	L_{forw} [$cm^{-2}s^{-1} \cdot 10^{30}$]	L_{back} [$cm^{-2}s^{-1} \cdot 10^{30}$]	Time [s]
3412	0.050 ± 0.002	0.038 ± 0.014	1596.9
3414	0.161 ± 0.006	0.121 ± 0.018	2064.4
3415	0.601 ± 0.022	0.440 ± 0.058	4117.6
3416	1.244 ± 0.046	0.970 ± 0.130	583.2
3417	0.687 ± 0.031	0.412 ± 0.125	84.4
3418	0.552 ± 0.019	0.405 ± 0.054	6923.4
3419	0.788 ± 0.028	0.582 ± 0.066	3386.5
3420	0.792 ± 0.028	0.580 ± 0.074	4023.15

Table 9. Luminosity for the beam energy 700 MeV (3 FMWPC).

Run number	L_{forw} [$cm^{-2}s^{-1} \cdot 10^{30}$]	L_{back} [$cm^{-2}s^{-1} \cdot 10^{30}$]	Time [s]
3438	0.343 ± 0.013	0.243 ± 0.078	1256.2
3439	0.407 ± 0.015	0.335 ± 0.062	2798.1
3440	0.369 ± 0.015	0.310 ± 0.060	2834.2
3441	0.464 ± 0.018	0.383 ± 0.093	3778.3
3442	0.455 ± 0.018	0.387 ± 0.061	3832.4
3443	0.379 ± 0.014	0.325 ± 0.067	4421.0
3453	0.228 ± 0.009	0.186 ± 0.034	7646.0
3454	0.478 ± 0.019	0.427 ± 0.060	3882.9
3455	0.495 ± 0.020	0.436 ± 0.080	3691.9
3456	0.438 ± 0.017	0.386 ± 0.066	2412.0
3457	0.195 ± 0.007	0.164 ± 0.031	8921.3
3458	0.462 ± 0.017	0.406 ± 0.060	3530.2
3459	0.505 ± 0.020	0.432 ± 0.048	1404.3

Table 10. Luminosity for the beam energy 800 MeV (3 FMWPC).

Run number	L_{forw} [$cm^{-2}s^{-1} \cdot 10^{30}$]	L_{back} [$cm^{-2}s^{-1} \cdot 10^{30}$]	Time [s]
3421	0.642 ± 0.027	0.600 ± 0.100	2601.2
3422	0.532 ± 0.022	0.471 ± 0.052	3688.3
3423	0.483 ± 0.019	0.376 ± 0.088	4648.9
3424	0.540 ± 0.020	0.409 ± 0.085	3078.4
3448	0.228 ± 0.009	0.235 ± 0.072	4414.8
3449	0.294 ± 0.011	0.226 ± 0.046	4836.1
3450	0.355 ± 0.014	0.312 ± 0.058	5280.8
3451	0.315 ± 0.013	0.251 ± 0.042	5314.7
3452	0.217 ± 0.009	0.193 ± 0.069	4544.4
3460	0.485 ± 0.020	0.396 ± 0.056	6681.7
3461	0.333 ± 0.025	0.226 ± 0.047	332.2
3462	0.469 ± 0.018	0.396 ± 0.035	7543.0
3463	0.403 ± 0.016	0.347 ± 0.061	2997.2

Table 11. Luminosity for the beam energy 950 MeV (3 FMWPC).

Run number	L_{forw} [$cm^{-2}s^{-1} \cdot 10^{30}$]	Time [s]
3430	0.022 ± 0.001	4718.7
3431	0.018 ± 0.001	1644.2
3433	0.022 ± 0.002	1645.5
3434	0.569 ± 0.024	3975.2
3435	0.457 ± 0.020	2697.6
3436	0.557 ± 0.024	4181.7
3437	0.490 ± 0.020	1429.0
3444	0.351 ± 0.015	3644.4
3445	0.352 ± 0.015	3526.3
3446	0.370 ± 0.016	3423.1
3447	0.376 ± 0.016	4268.6

Table 12. Luminosity for the beam energy 1350 MeV (3 FMWPC).

Run number	L_{forw} [$cm^{-2}s^{-1} \cdot 10^{30}$]	Time [s]
3425	0.580 ± 0.023	2265.1
3426	0.486 ± 0.018	3824.4
3427	0.392 ± 0.015	3664.9
3428	0.500 ± 0.018	301.8
3429	0.389 ± 0.014	4569.3

Table 13. Luminosity for the beam energy 1900 MeV (3 FMWPC).

Run number	L_{forw} [$cm^{-2}s^{-1} \cdot 10^{30}$]	Time [s]
3407	0.297 ± 0.012	1861.8
3408	0.432 ± 0.018	3910.7
3409	0.360 ± 0.014	4616.9
3410	0.700 ± 0.029	2169.1
3411	1.212 ± 0.052	1342.3

Table 14. Correction factors and uncertainties.

	Correction factor
Efficiency of the FD trigger, $E_{trgig} = 97.6\%$	1.024 ± 0.012
D2 exit window cut	1.01 ± 0.005 $(9^0 < \Theta < 10^0)$
Cut in the minimal mass spectrum	1.002
MWPC efficiency correction	1.00 ± 0.03
Low momentum cut in the momentum spectra	1.025 ± 0.01
Theoretical differential cross section uncertainty	1.0 ± 0.1

Table 15. Comparison of luminosity determined by pd forward and backward scattering using 2 FMWPC and 3 FMWPC track reconstruction algorithms.

T_p	L_{forw} (2PC)	L_{forw} (3PC)	L_{back} (2PC)	L_{back} (3PC)
[MeV]	$[\mathrm{cm}^{-2}s^{-1} \cdot 10^{30}]$	$[\mathrm{cm}^{-2}s^{-1} \cdot 10^{30}]$	$[\mathrm{cm}^{-2}s^{-1} \cdot 10^{30}]$	$[\mathrm{cm}^{-2}s^{-1} \cdot 10^{30}]$
600	0.491 ± 0.021	0.586 ± 0.021	0.409 ± 0.072	0.432 ± 0.056
700	0.311 ± 0.018	0.364 ± 0.014	0.308 ± 0.057	0.304 ± 0.050
800	0.356 ± 0.021	0.404 ± 0.016	0.345 ± 0.079	0.358 ± 0.070
950	0.310 ± 0.015	0.345 ± 0.014	-	-
1350	0.404 ± 0.024	0.447 ± 0.017	-	-
1900	0.471 ± 0.035	0.507 ± 0.021	-	-

Table 16. Integral luminosity summary table (3FMWPC).

T_p, MeV	$\int L_{forw} dt$ $[\mathrm{cm}^{-2} \cdot 10^{34}]$
600	1.406 ± 0.050
700	1.934 ± 0.074
800	2.382 ± 0.094
950	1.284 ± 0.053
1350	0.689 ± 0.025
1900	0.743 ± 0.031

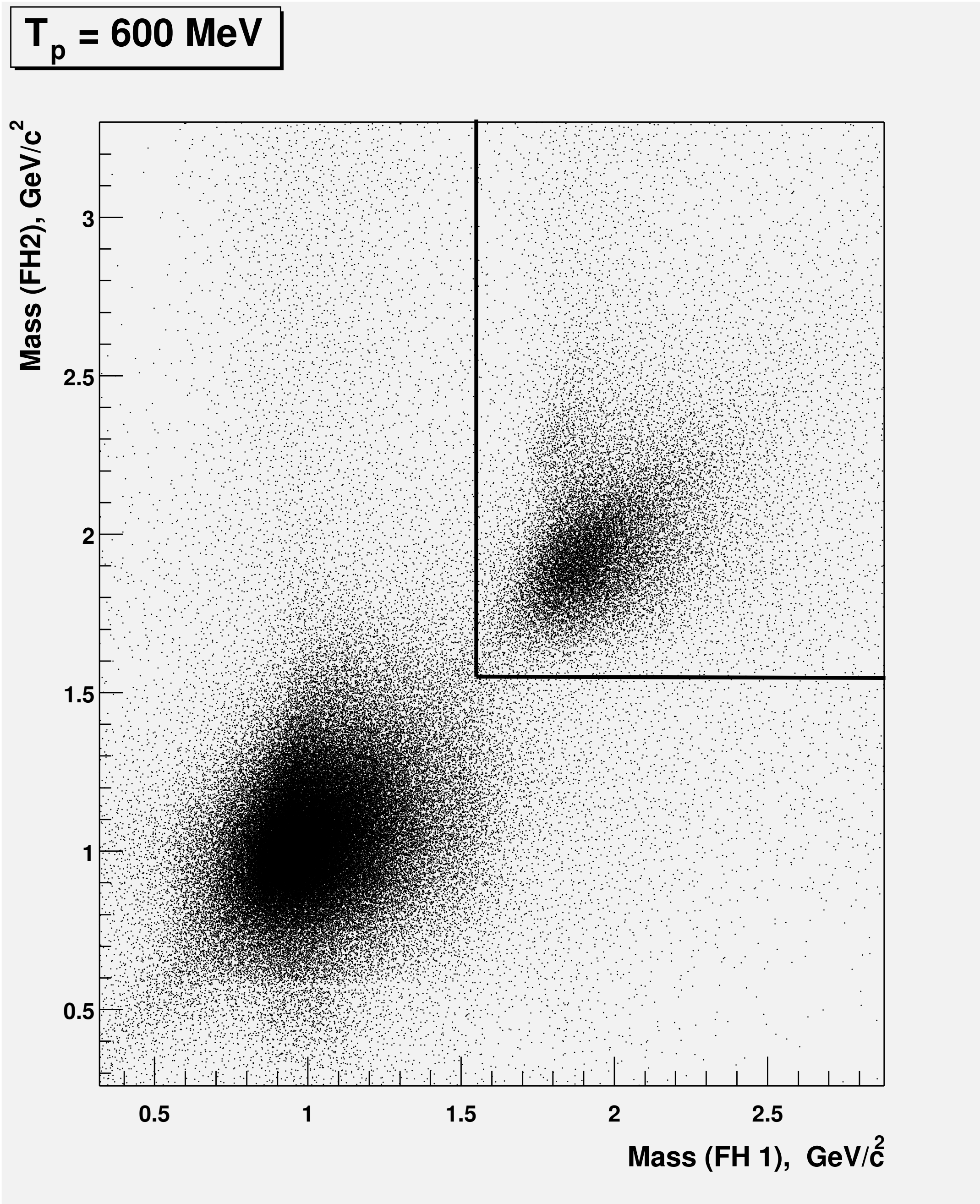

Figure 1: Particle mass calculated by energy losses in the first plane of Forward hodoscope versus particle mass calculated by energy losses in second plane.

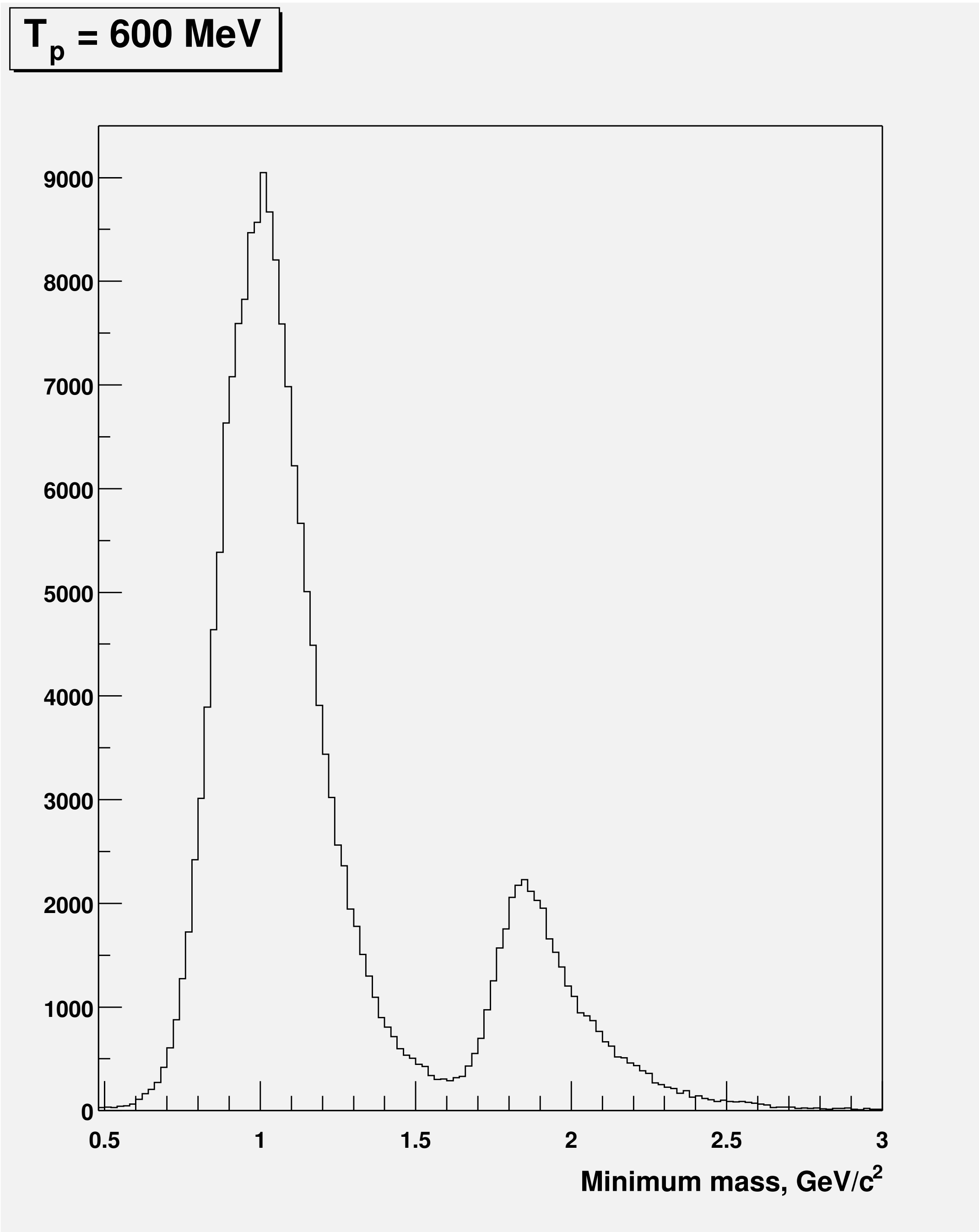

Figure 2: Distribution of minimal mass.

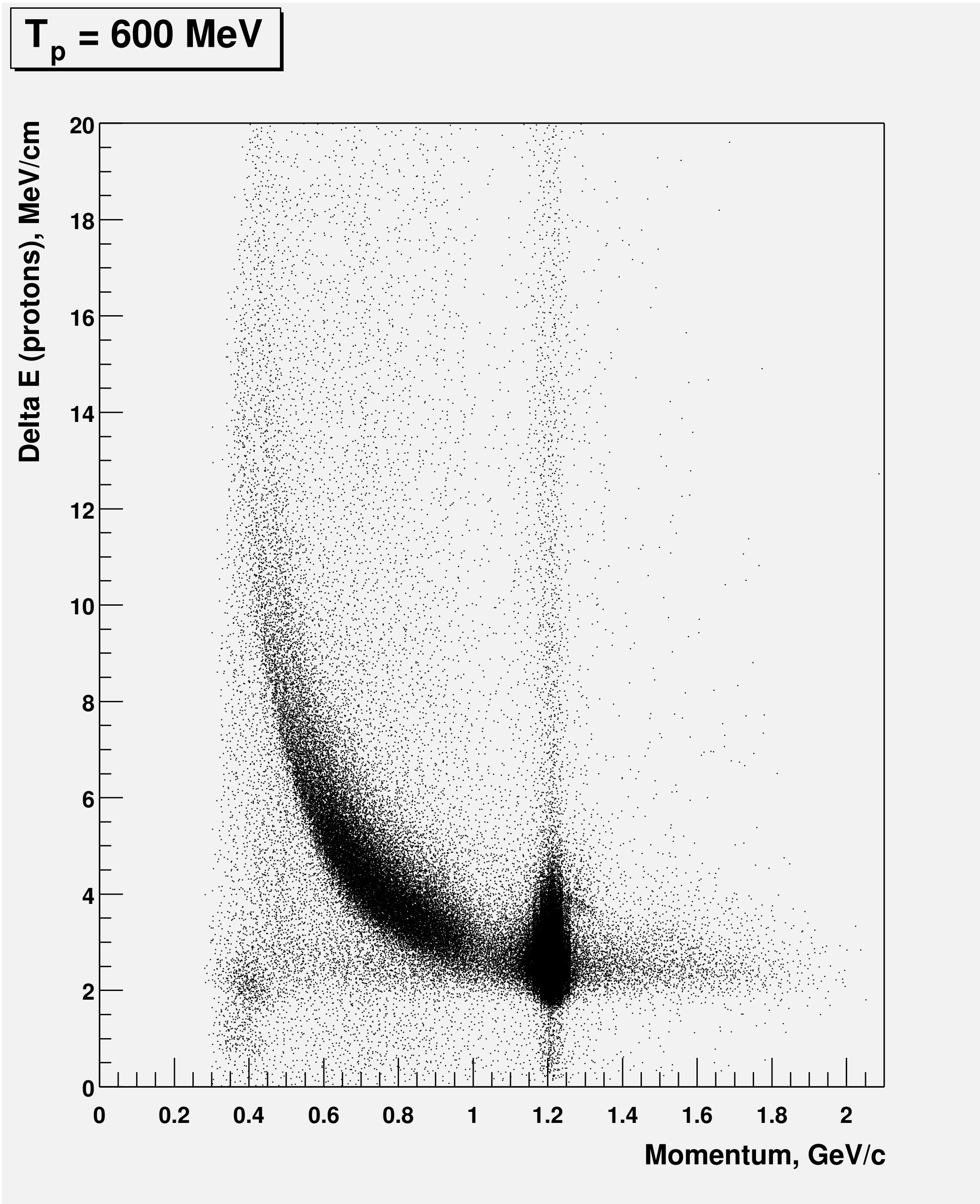

Figure 3: Energy losses — momentum distribution for protons selected using minimal mass criterion.

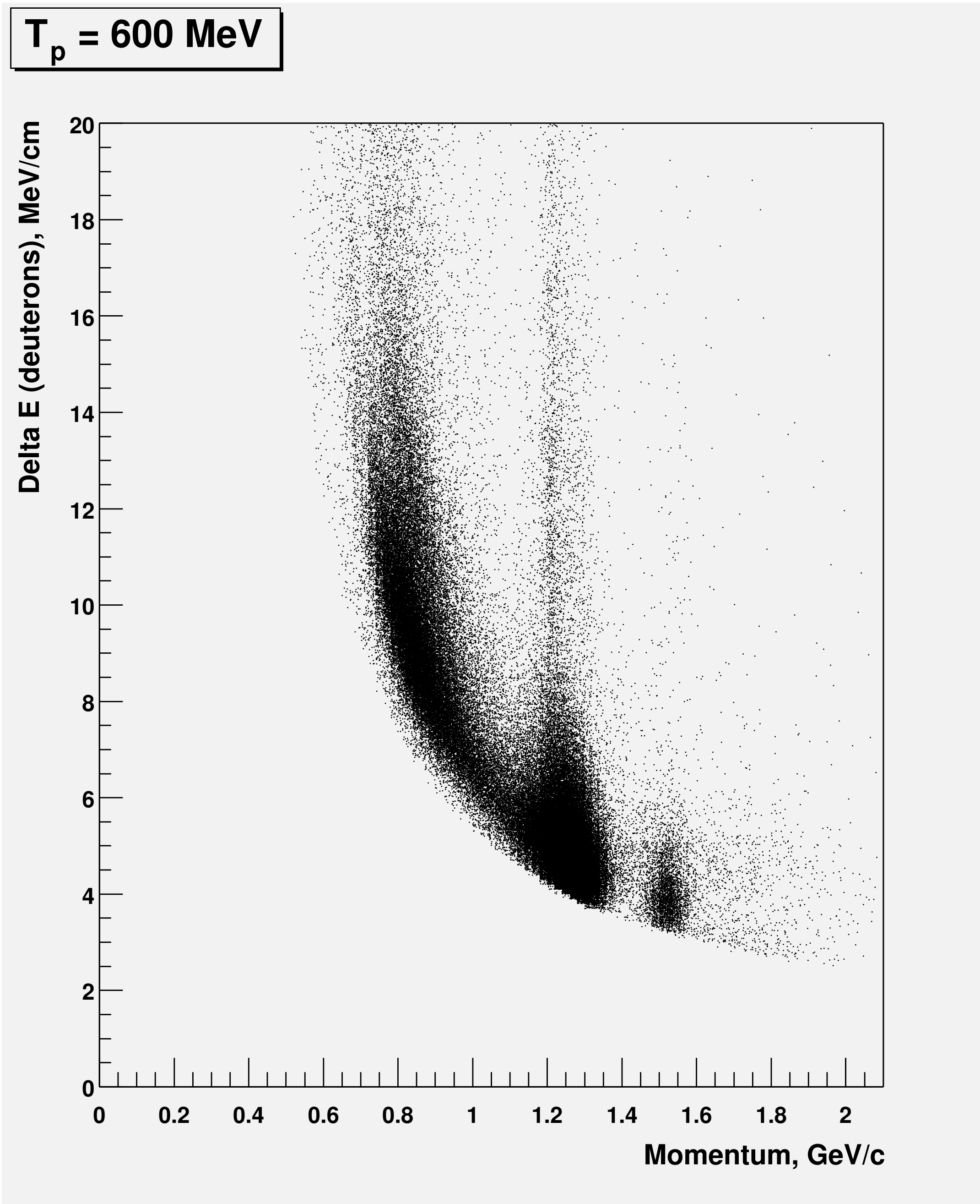

Figure 4: Energy losses — momentum distribution for deuterons selected using minimal mass criterion.

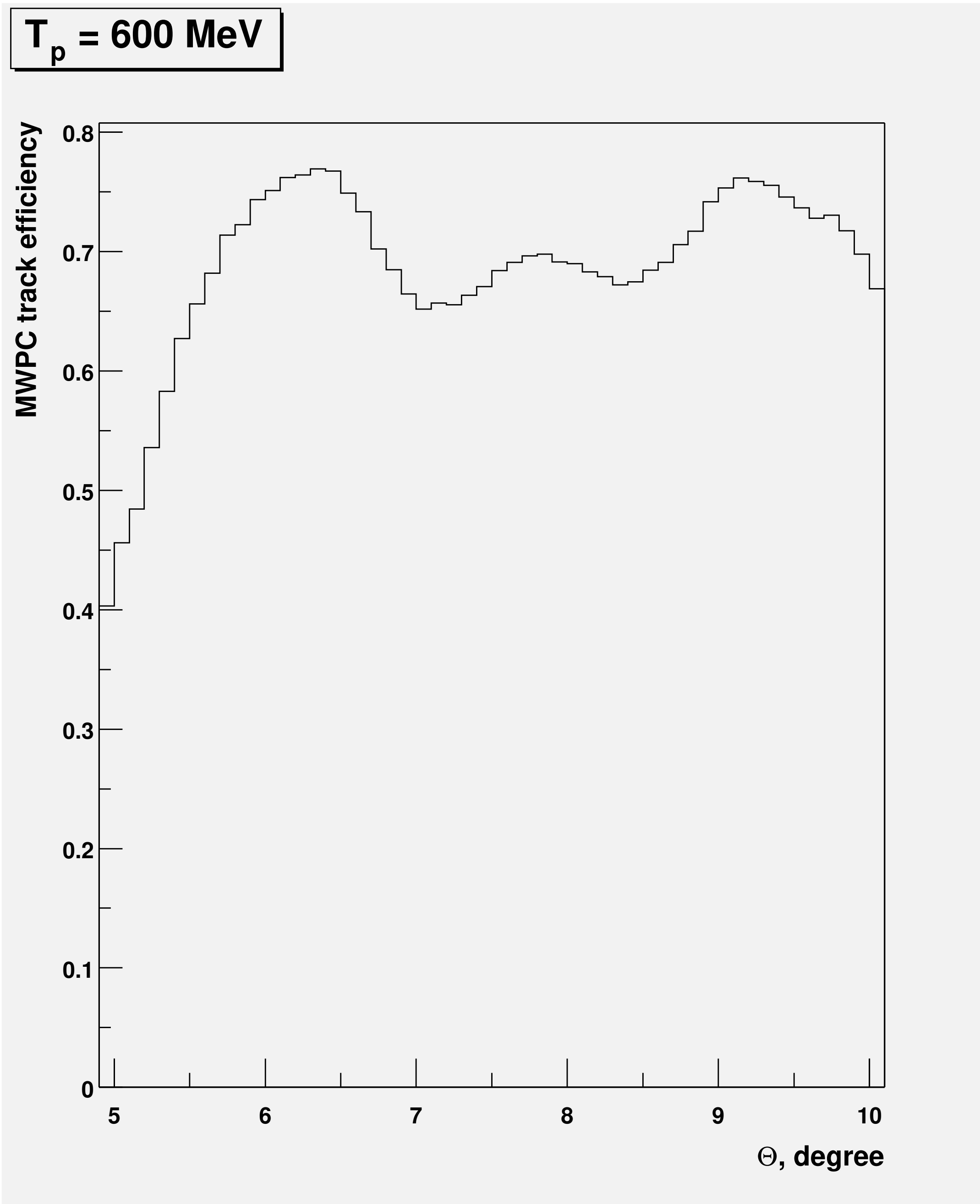

Figure 5: Track efficiency dependence on the polar angle for the *pd* forward scattering reaction events (2 FMWPC track reconstruction algorithms).

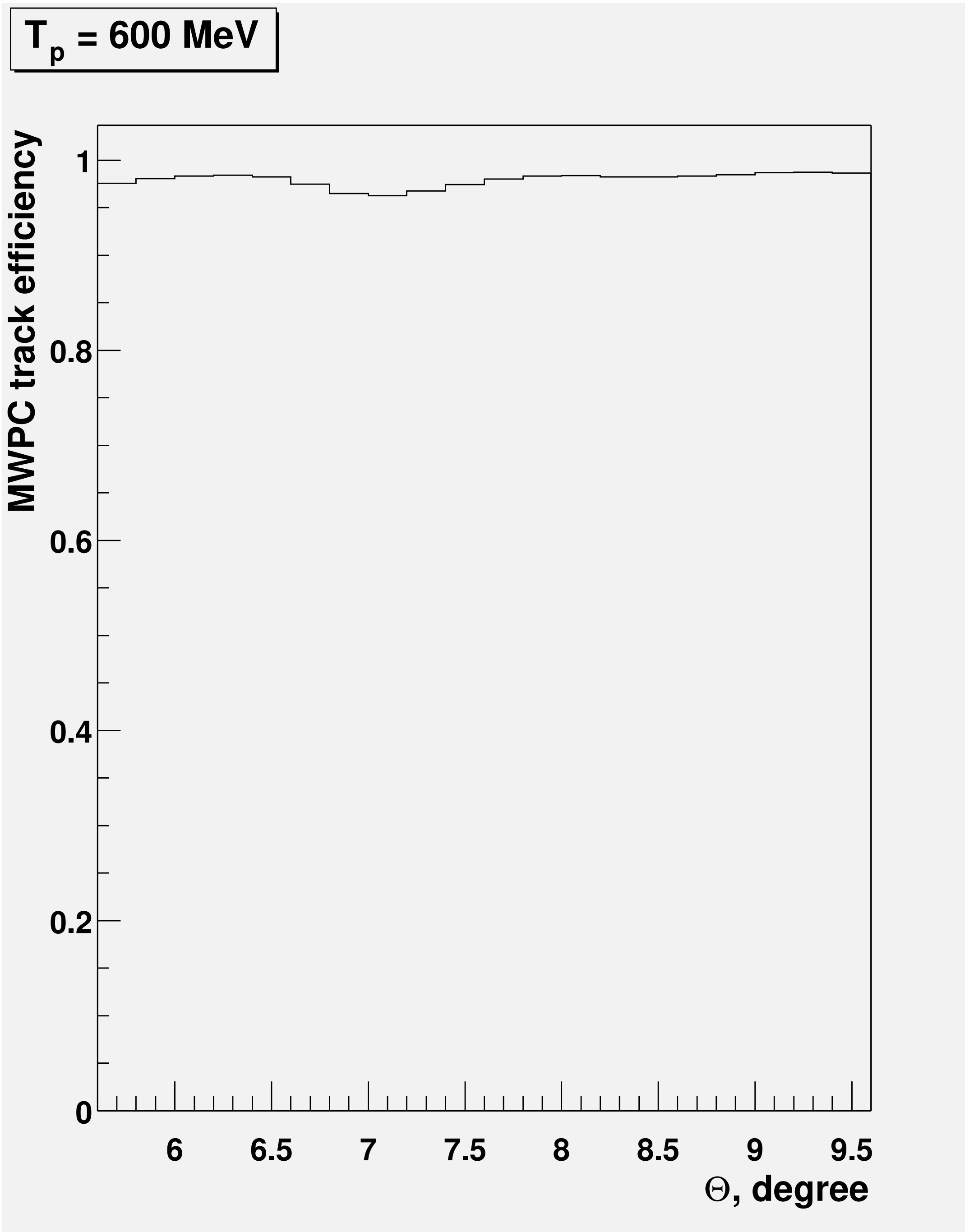

Figure 6: Track efficiency dependence on the polar angle for the *pd* forward scattering reaction events (3 FMWPC track reconstruction algorithms).

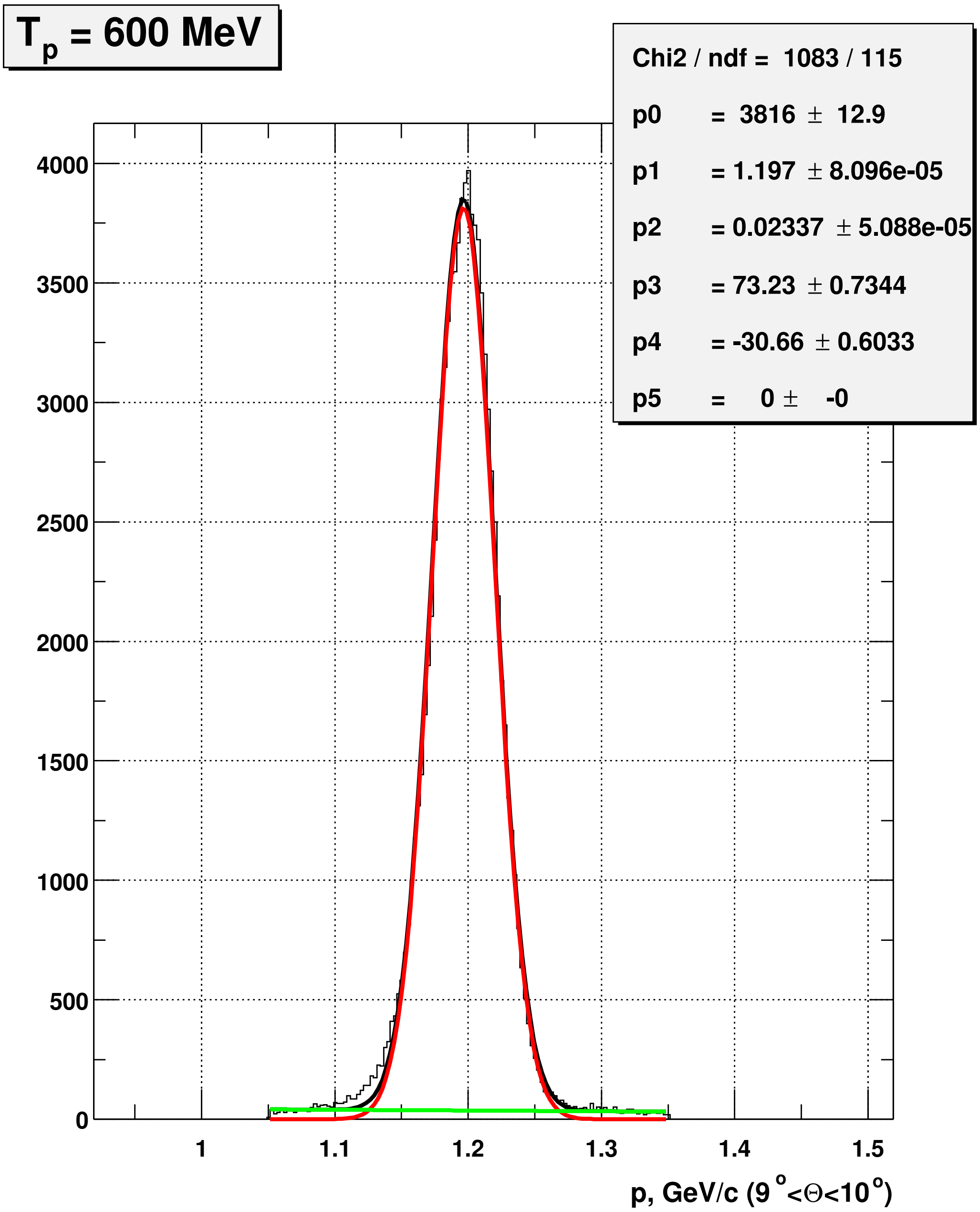

Figure 7: Momentum spectra of protons from *pd* forward scattering after selection by energy losses.

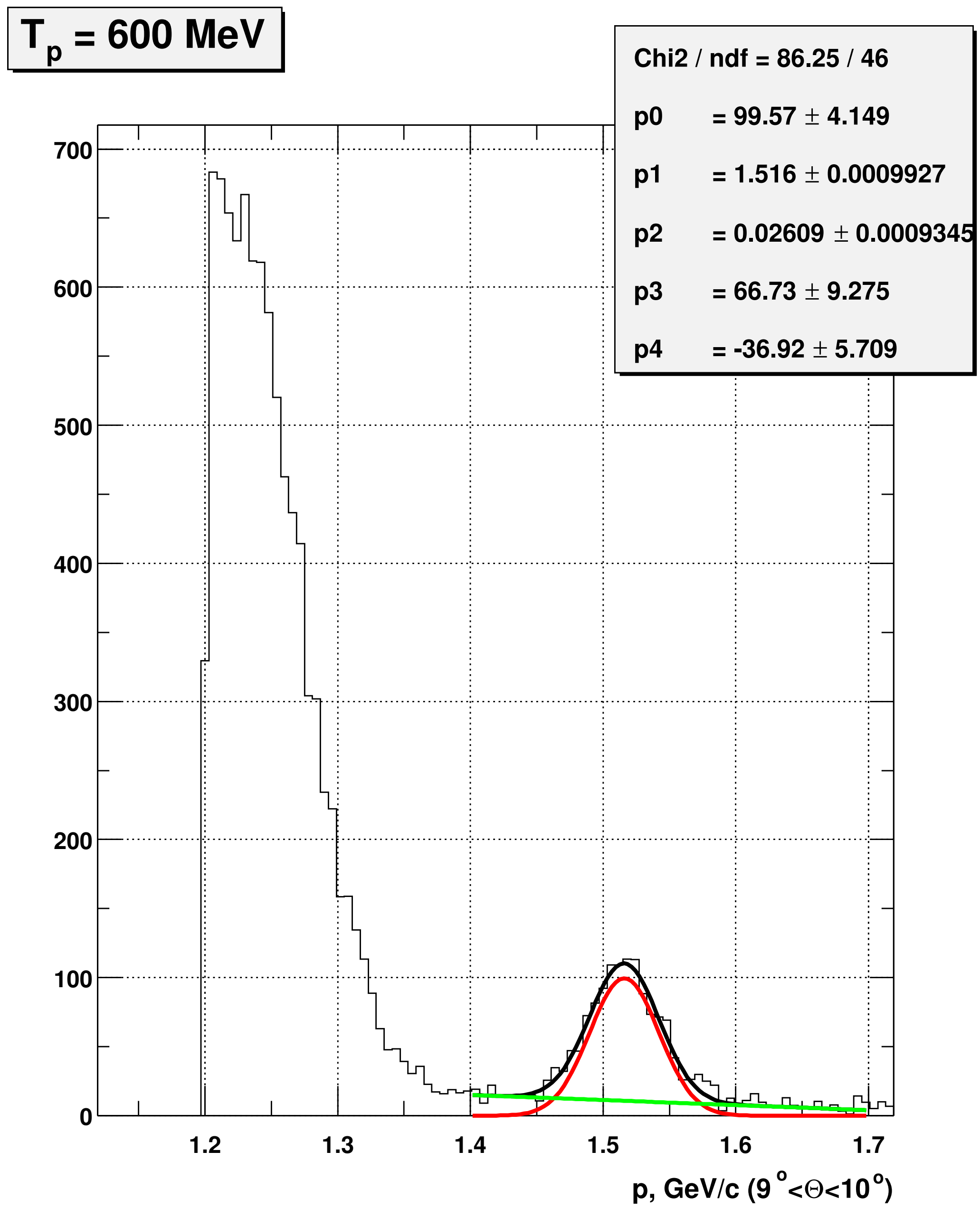

Figure 8: Momentum spectra of deuterons from pd backward scattering after selection by energy losses.

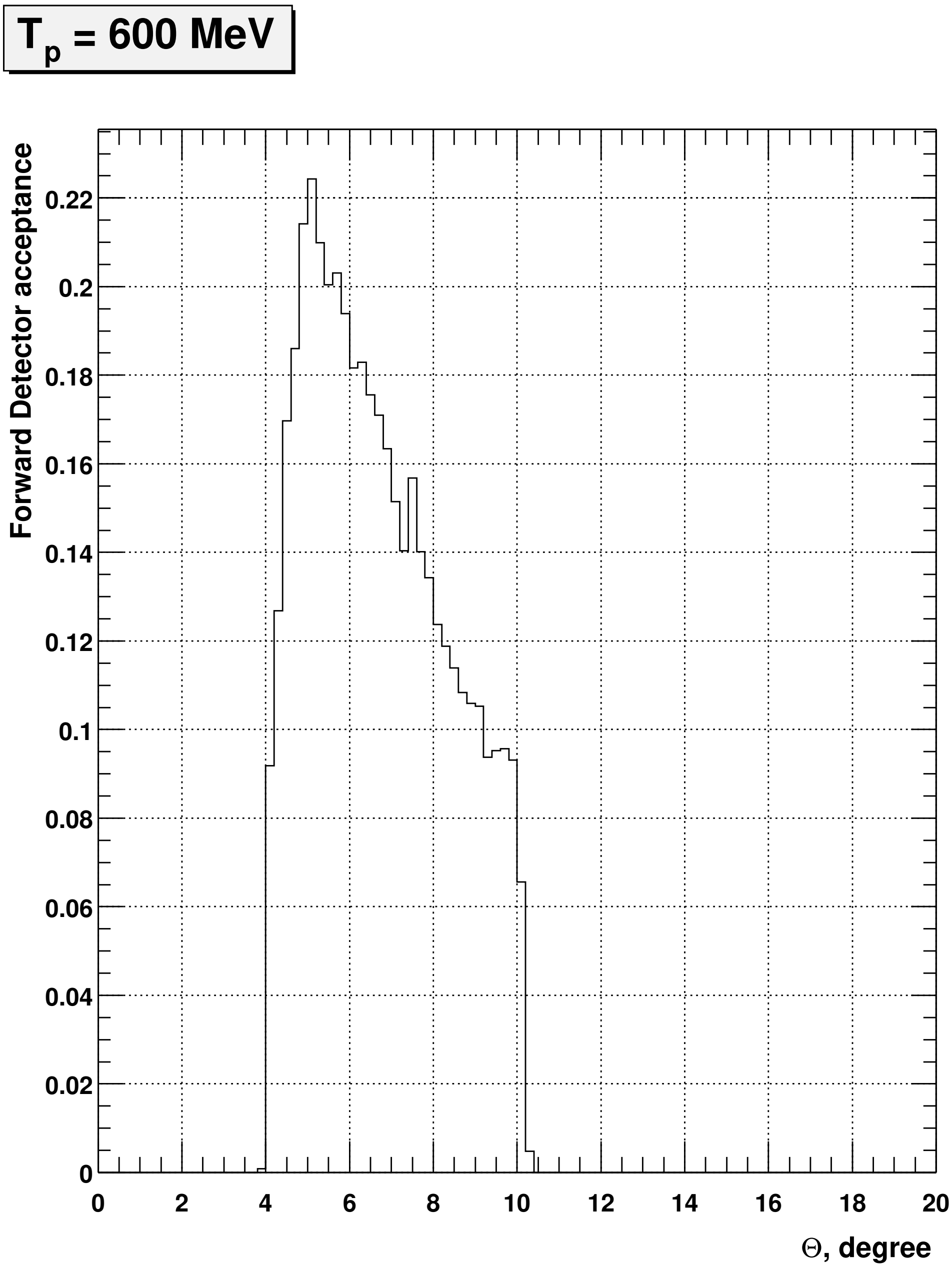

Figure 9: FD acceptance of pd elastic.

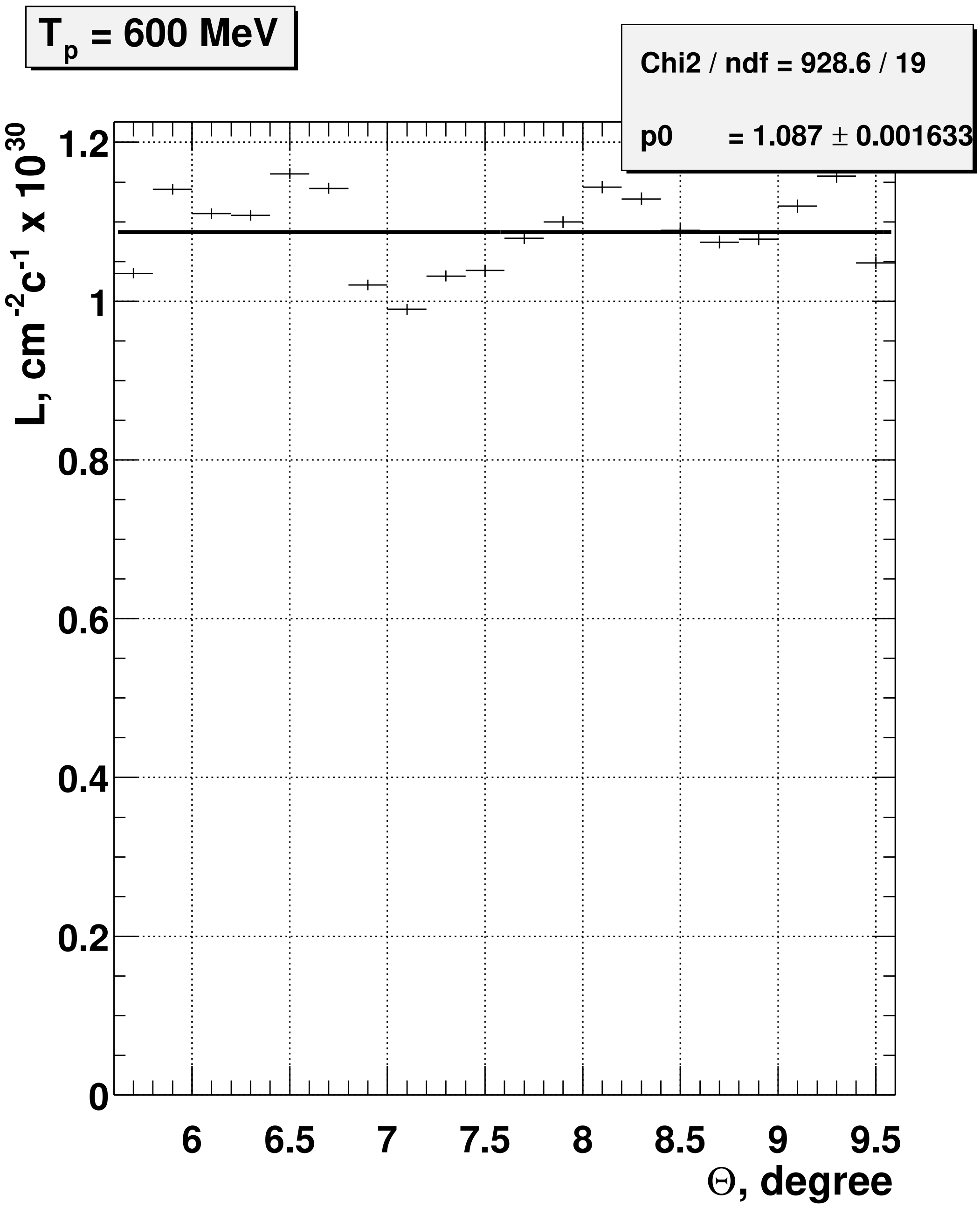

Figure 10: Luminosity angular dependence for *pd* forward scattering (2 FMWPC track reconstruction algorithms).

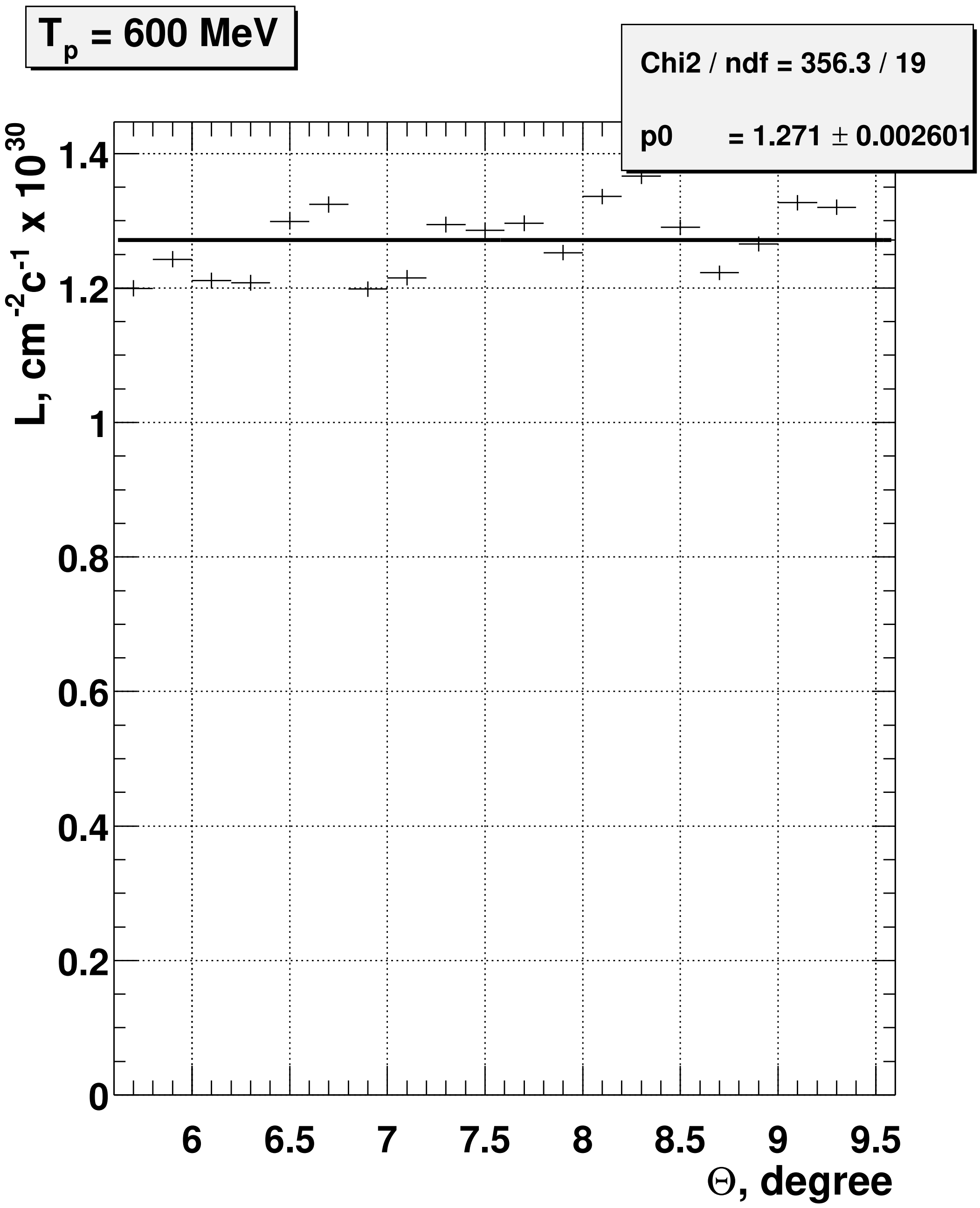

Figure 11: Luminosity angular dependence for *pd* forward scattering (3 FMWPC track reconstruction algorithms).

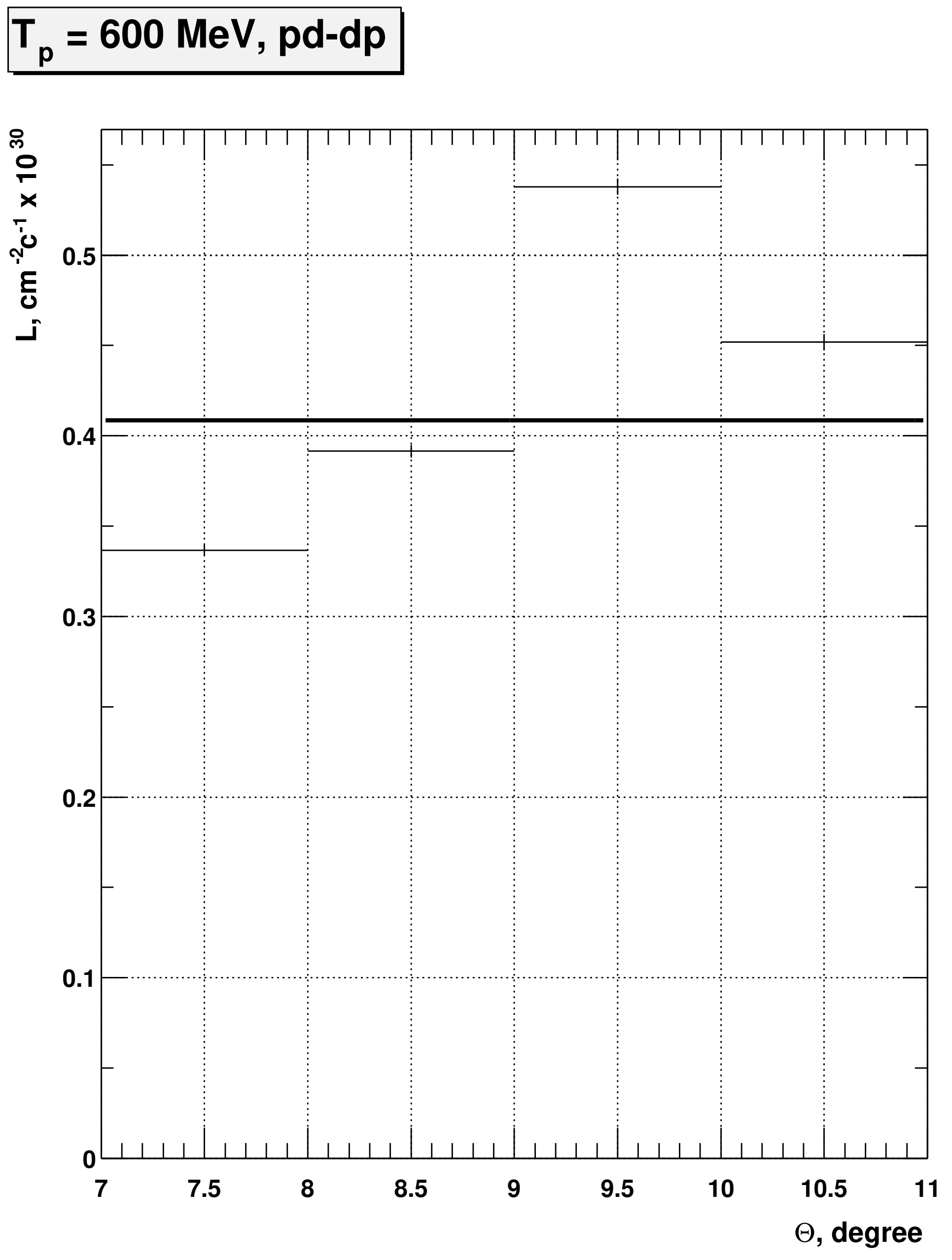

Figure 12: Luminosity angular dependence for pd backward scattering.

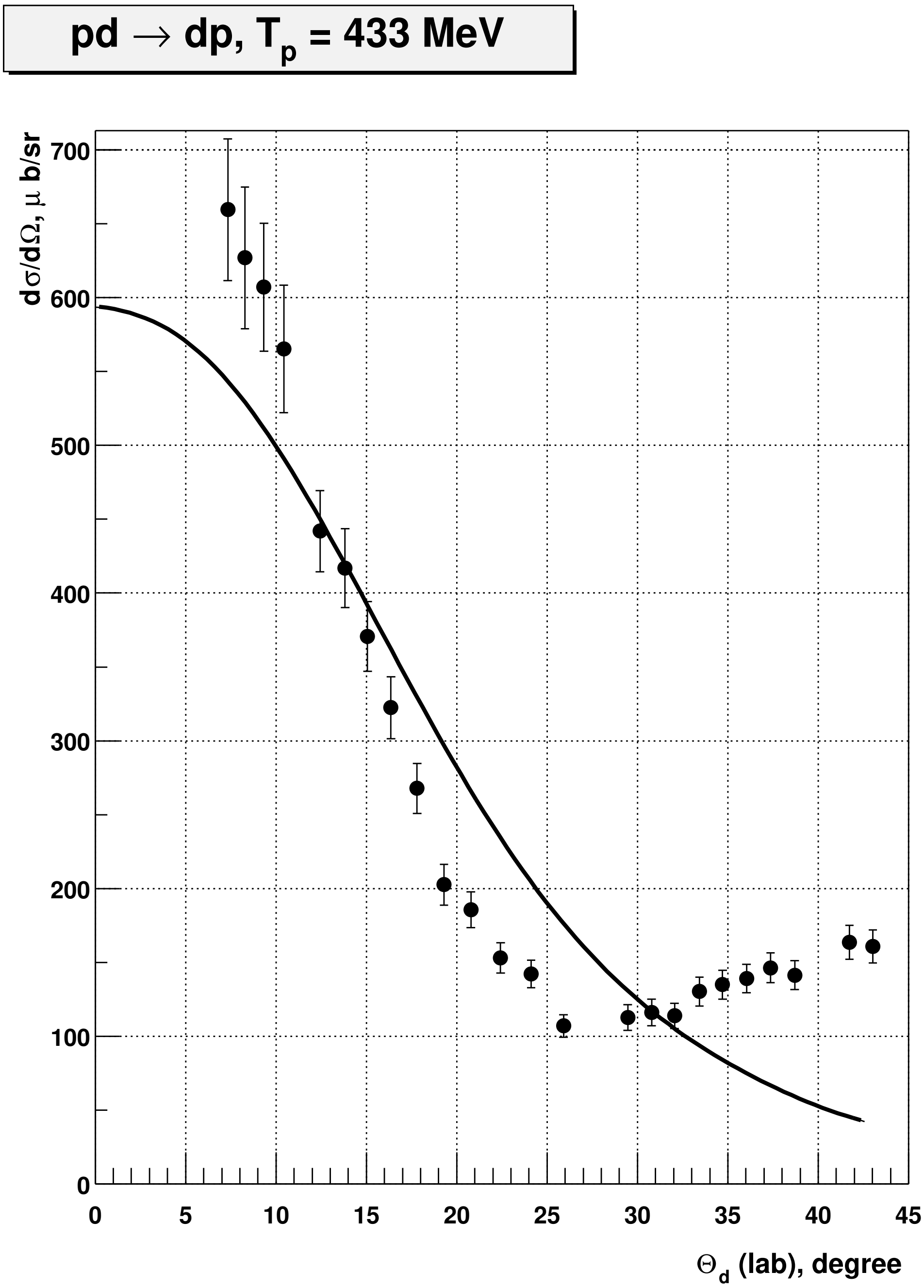

Figure 13: Comparison of experimental data on *pd* backward elastic scattering with theoretical calculations.

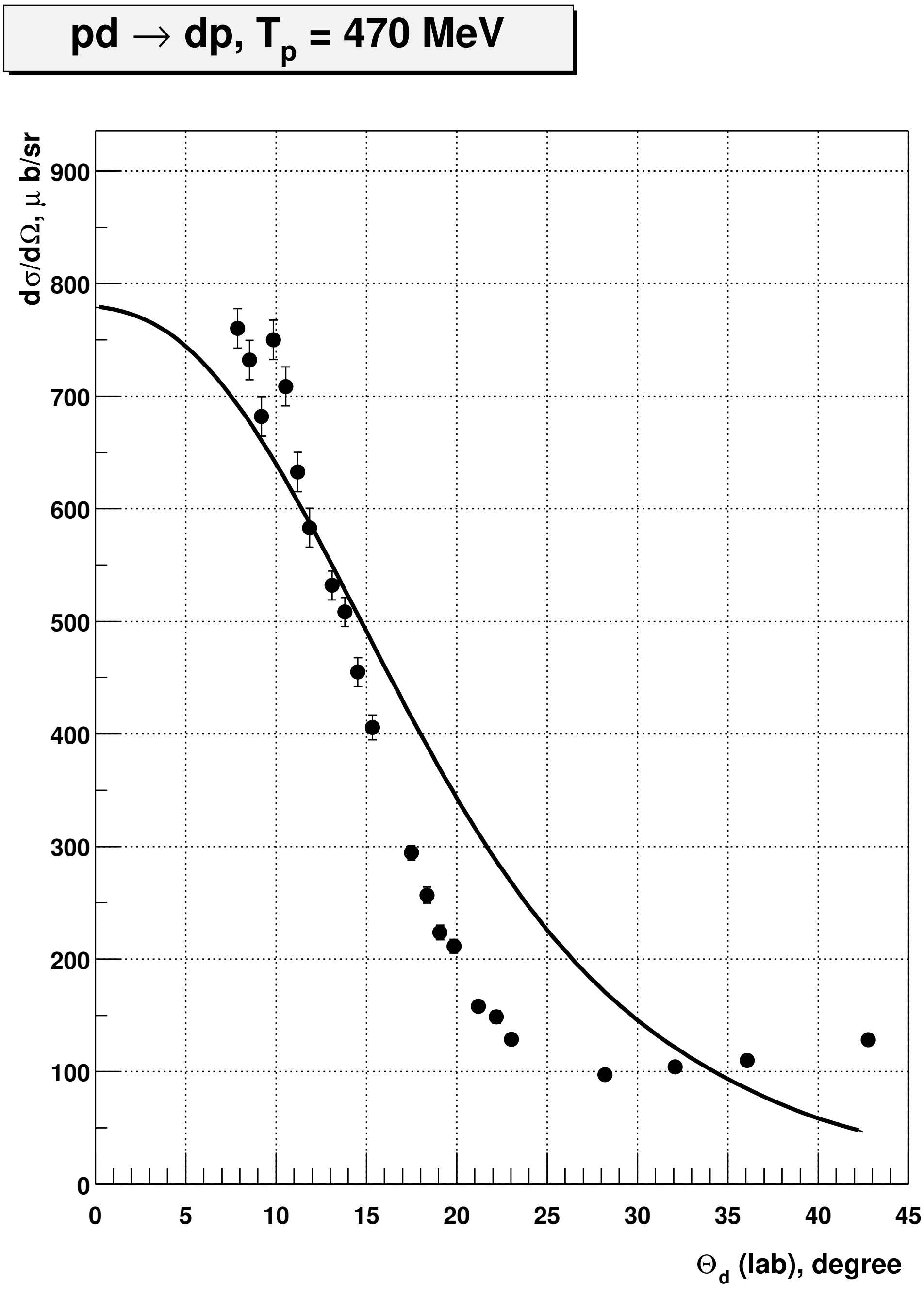

Figure 14: Comparison of experimental data on *pd* backward elastic scattering with theoretical calculations.

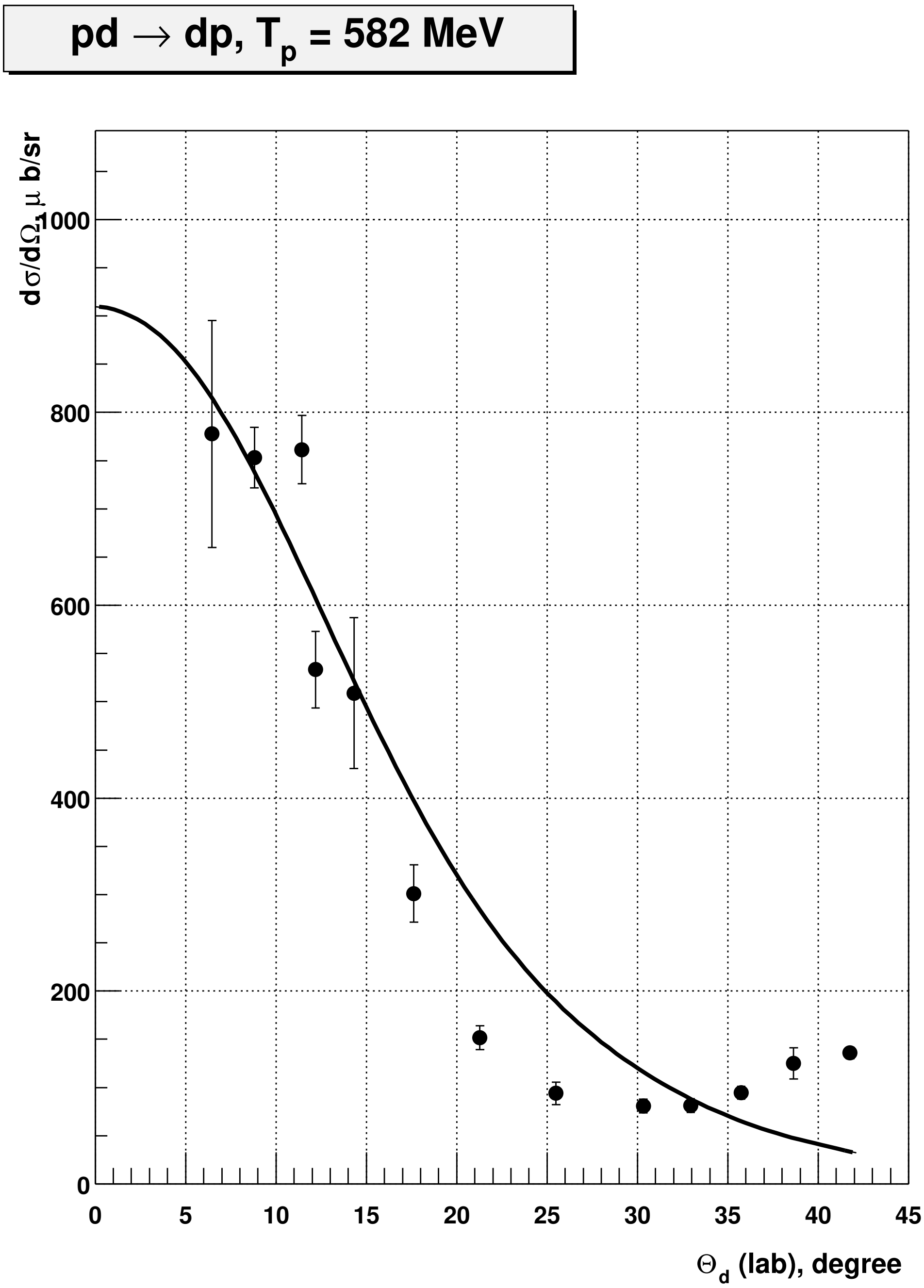

Figure 15: Comparison of experimental data on *pd* backward elastic scattering with theoretical calculations.

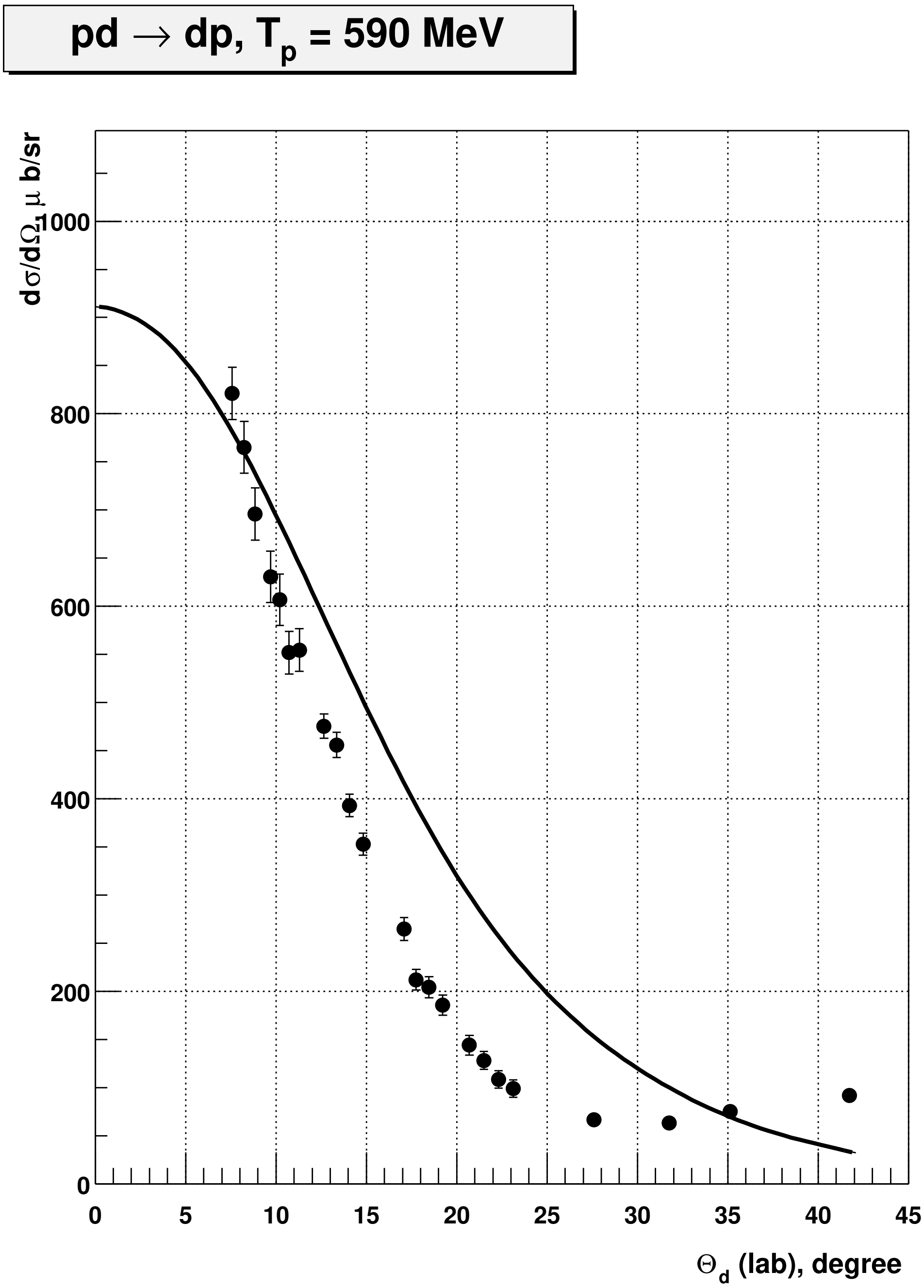

Figure 16: Comparison of experimental data on *pd* backward elastic scattering with theoretical calculations.

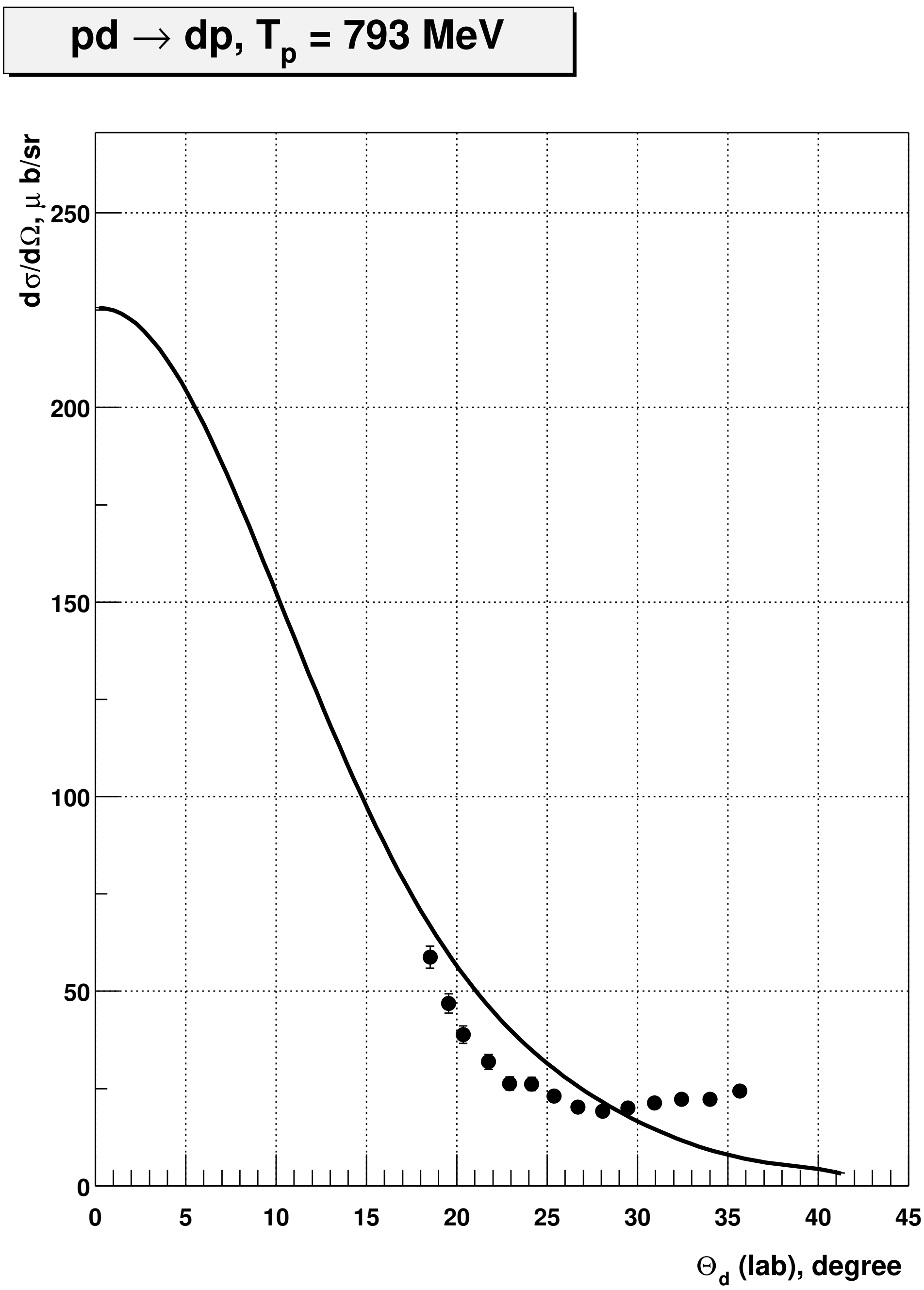

Figure 17: Comparison of experimental data on *pd* backward elastic scattering with theoretical calculations.

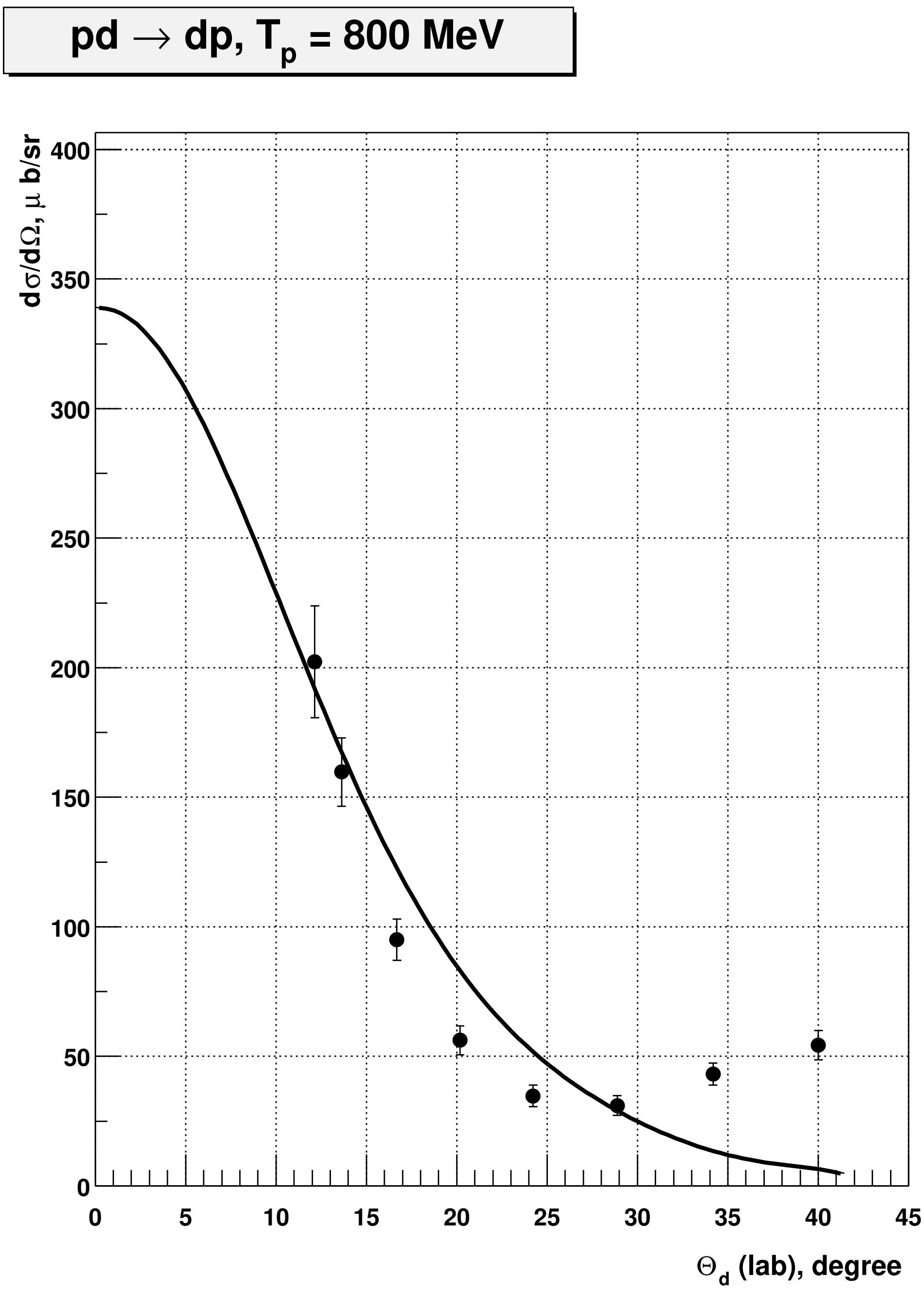

Figure 18: Comparison of experimental data on *pd* backward elastic scattering with theoretical calculations.